

# A Fundamental Wax Deposition Model for Water-in-Oil Dispersed Flows in Subsea Pipelines

Sheng Zheng  and H. Scott Fogler

Dept. of Chemical Engineering, University of Michigan, Ann Arbor, MI 48109

Amir Haji-Akbari

School of Engineering and Applied Science, Yale University, New Haven, CT 06520

DOI 10.1002/aic.15750

Published online April 22, 2017 in Wiley Online Library (wileyonlinelibrary.com)

*Water-in-oil dispersions frequently form in subsea oil pipeline transportation and their presence affects the wax deposition rate in subsea pipelines. A fundamental model for wax deposition on the wall of water-in-oil dispersed phase flow pipelines has not been developed. Dispersed water droplets can affect the heat and mass transfer characteristics of wax deposition and alter the deposit growth rate. In this study, wax deposition from water-in-oil dispersed flows is comprehensively modeled using first principles of heat and mass transfer. The role of the dispersed water phase on the heat and mass transfer aspects of wax deposition is analyzed. The developed model predicts different effects of the water volume fraction and droplet size on the wax deposition rates in laboratory flow loop experiments and in field scale wax deposition processes.* © 2017 American Institute of Chemical Engineers *AICHE J*, 63: 4201–4213, 2017

*Keywords: computational fluid dynamics (CFD), energy, heat transfer, mass transfer, wax deposition*

## Introduction

Wax deposition in subsea oil pipelines is a challenging problem in off-shore oil transportation as it causes a reduction in the cross-sectional area available for oil flow, thereby increasing the required pump pressure to maintain a specified production rate. If the wax deposit is not removed periodically by the costly pigging operations, it can grow to too thick and hard and become virtually impossible to be removed by pigging, such as the case shown in Figure 1.

Under such extreme circumstances, the only way to resume production is to dispatch deep sea divers to cutoff the clogged pipe section at the cost of 10 of millions of dollars.<sup>1</sup> However, excessively frequent pigging operations pose a severe economic burden on the upstream oil industry. With the status of the global oil market, even the major operators must be extremely cautious when determining the pigging frequency. Knowledge of wax deposition rates and thicknesses in subsea pipelines is crucial to the proper scheduling of pigging operations. As a result, a substantial number of theoretical and experimental studies<sup>1–10</sup> have been conducted to understand the physics of wax deposition and to predict the deposit growth rate and thickness. Previous modeling studies focused mostly on single phase oil flows.<sup>1,7–10</sup> However, multiphase flows, including oil–gas/oil–water two phase flows and oil–gas–water three phase flows can occur in oil field operations.

Fundamental wax deposition models for multiphase flow patterns have not been developed. Among the multiphase flow scenarios, oil–water two phase flows have gained increasing interests from the upstream oil industry as the water content of the production stream continues to increase as production time of a reservoir elapses. Among the possible oil–water flow patterns, such as water-in-oil dispersed flow, oil-centered annular flow, stratified flow and oil-in-water dispersed flow,<sup>11</sup> wax deposition can occur from water-in-oil dispersed phase flow and stratified flow because in these two flow patterns, the pipe wall is completely or partly in contact with the oil phase. Huang et al. developed a fundamental wax deposition model for oil–water stratified channel flow.<sup>12</sup> The transportation of oil in most pipelines occurs in turbulent flow regime and the turbulent eddies intensively mix oil and water. In comparison with water–oil stratified flow, water-in-oil dispersed flow is a common flow pattern in field operations as intensive mixing and the presence of natural surfactants<sup>13–16</sup> together promote the formation of water-in-oil dispersion. Nevertheless, no fundamental wax deposition model for this flow pattern has been developed. The only wax deposition modeling study regarding water-in-oil dispersed flow, by Bruno et al., uses the pseudo-single phase (PSP) approach to model flow loop deposition experiments.<sup>17</sup> In this investigation, the heat and mass transfer characteristics of wax deposition were analyzed using first principles from transport theories. For heat transfer simulation, in addition to the pseudosingle phase approach used by Bruno et al.,<sup>18</sup> the two phase Eulerian–Eulerian method was applied. Comparisons between the simulation results from the two approaches for heat transfer modeling provide a guideline to select heat transfer model in wax deposition analysis. For mass transfer simulation, reliable approaches to calculate the

Additional Supporting Information may be found in the online version of this article.

Correspondence concerning this article should be addressed to H. S. Fogler at sfogler@umich.edu.

© 2017 American Institute of Chemical Engineers

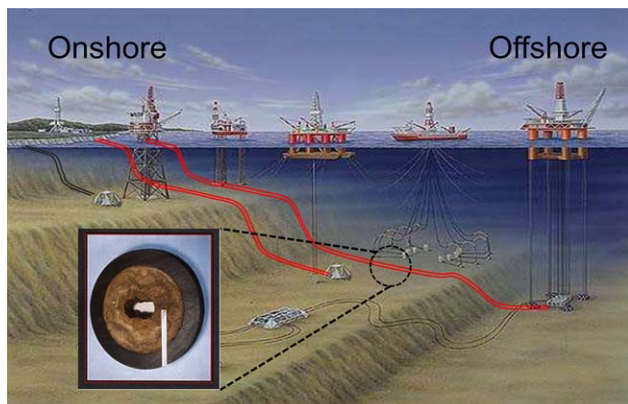


**Figure 1. A schematic of the layout of subsea pipelines and a cross-section of the pipeline plugged by wax deposit.**

[Color figure can be viewed at [wileyonlinelibrary.com](http://wileyonlinelibrary.com)]

radial diffusive flux of wax were established based on the unique diffusion characteristic of wax in water-in-oil dispersion, that is, diffusion occurs around the water droplets. The wax deposition model combining the heat and mass transfer characteristics in water-in-oil dispersed flow was applied not only to model lab scale wax deposition experiments but also field scale wax deposition. The roles of the water volume fraction and droplet size on wax deposition are uncovered with theoretical analysis.

### Introduction of Wax Deposition Modeling for Water-in-Oil Dispersed Flows

The wax deposition model developed in this work is based on the Michigan Wax Predictor<sup>7</sup> and consists of four sequential calculation steps: (1) a hydrodynamic calculation, (2) a heat transfer calculation, (3) a mass transfer calculation, and (4) a deposit growth calculation. At each time step  $t$ , the velocity profile of the oil–water mixture is first obtained based on the universal velocity profile for turbulent flow and the parabolic velocity profile for laminar flow. The velocity profile together with the water content and the droplet size distribution will be used as input parameters for the heat and mass transfer calculations to determine the temperature and dissolved wax concentration profiles. Figure 2 shows a schematic of the unique heat and mass transfer characteristics associated with the water-in-oil dispersed flow.

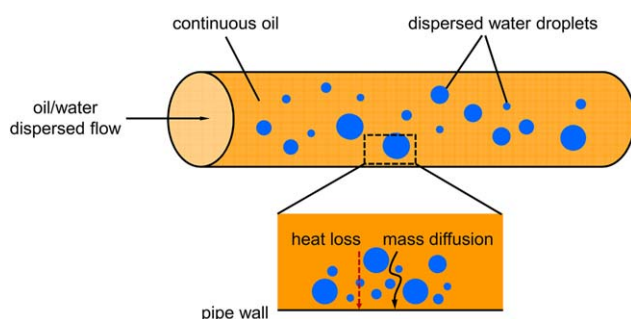


**Figure 2. A schematic summarizing the heat and mass transfer characteristics for wax deposition in water-in-oil dispersed flow.**

[Color figure can be viewed at [wileyonlinelibrary.com](http://wileyonlinelibrary.com)]

As can be seen from Figure 2, heat conduction from the flow to the cold wall can occur through water droplets. Different from heat transfer, mass transfer *cannot* occur through the droplets as wax molecules cannot dissolve in water droplets and therefore must diffuse around them. Based on the dissolved wax concentration profile, the radial flux of wax is calculated to obtain the deposit growth rates. The computational grid is updated at the end of each cycle to account for the formation of a deposit layer and a new computational grid is used in the next time step,  $t + \Delta t$ . This calculation procedure is repeated until the simulation time reaches a specified duration for wax deposition. Detailed mathematical formulations of the modifications for the two-phase heat and mass transfer characteristics will be presented in the following sections.

### Hydrodynamic Calculations

Predicting the velocity profile in water-in-oil dispersions is essential to subsequent heat and mass transfer calculations because “velocity” is an input parameter to solve the governing heat and mass transfer equations. In carrying out the hydrodynamic calculations, it can be assumed that, owing to their small sizes, the dispersed water droplets move at the same velocity as the continuous oil phases. This assumption is realistic and significantly simplifies the mathematical formulation of the hydrodynamic calculations. This assumption can be justified by the following argument. Hypothetically, if a water droplet moves at a velocity different from that of the surrounding oil, the drag force from the oil phase will quickly accelerate or decelerate the droplet until the velocity difference is eliminated. For example, with a typical oil phase viscosity of 10 c.P., it requires only  $\sim 0.1$  second to accelerate a 1-mm diameter droplet from stationary to reach 99% the velocity of the surrounding oil. A typical water-in-crude oil emulsion contains droplets that are smaller than 1 mm<sup>18,19</sup> and it then requires even less than 0.1 s for the droplet to be accelerated to virtually the same velocity as the surrounding oil.

Because of the negligible local velocity difference between the oil and water phases, these two phases can be lumped into a single pseudophase whose velocity profile can be used to represent the velocity profiles of both phases. Equations from the original single phase MWP were used to calculate the velocity profile with the viscosity of the water-in-oil dispersion mixture replacing that of the oil. Detailed equations for the hydrodynamic calculations can be found in the study by Huang et al.<sup>7</sup> and thus will not be repeated here. These equations were also included in Supporting Information Appendix A.

### Heat Transfer Calculations

Heat transfer models are used to calculate the temperature profile of the oil, which will be used as the input for the calculation of concentration profile of dissolved wax. Two approaches can be used to perform the heat transfer modeling: the pseudosingle phase (PSP) approach<sup>18</sup> and the Eulerian–Eulerian (E-E) approach.<sup>20</sup> Detailed mathematical formulations of both approaches will be introduced in the subsections. The E-E approach is theoretically rigorous although computationally intensive. Under certain operating conditions, such as fine droplet diameter and slow heat loss rate to the ambient, the computationally efficient PSP model can be used without causing significant error. Comparison between the PSP and E-E models under various operating conditions will be shown in this section as well.

### Eulerian–Eulerian (E-E) approach

The Heat Transfer Governing Equations and Boundary Conditions. The Eulerian–Eulerian (E-E) approach uses two variables,  $T_o(r, z)$  and  $T_w(r, z)$  to describe the oil and water temperature profiles. To determine  $T_o$  and  $T_w$ , two sets of governing heat transfer equations and boundary conditions need to be solved. The governing equation of the oil phase is

$$\text{oil phase : } \rho_o C_{p_o} \phi_o V_z \frac{\partial T_o}{\partial z} + \phi_o \frac{1}{r} \frac{\partial}{\partial r} \left[ -r \left( k_o + C_{p_o} \frac{\mu_T}{Pr_T} \right) \frac{\partial T_o}{\partial r} \right] - h_{\text{inter}} (T_w - T_o) = 0 \quad (1)$$

where

- $T_o(K)$  = oil temperature
- $T_w(K)$  = water temperature
- $\rho_o(kg/m^3)$  = density of oil
- $C_{p_o}(J/kg/K)$  = heat capacity of oil
- $\phi_o$  = volume fraction of oil
- $V_z(m/s)$  = axial velocity
- $z(m)$  = axial position
- $r(m)$  = radial position
- $k_o(W/m/K)$  = thermal conductivity of oil
- $\mu_T(Pa \cdot s)$  = turbulent viscosity
- $Pr_T$  = turbulent Prandtl number
- $h_{\text{inter}}(W/m/K)$  = heat transfer coefficient between oil and water

The first term on the left-hand side of Eq. 1 represents the energy flow by advection in the axial direction. The second term represents the heat transfer in the radial direction. Enhanced heat transfer due to turbulent eddies is accounted for by the addition of eddy thermal conductivity,  $k_{o,T} = C_{p_o} \frac{\mu_T}{Pr_T}$ , to the material thermal conductivity,  $k_o$ .

The first two terms in Eq. 1 are also present in the heat transfer governing equation for single phase wax deposition modeling.<sup>13</sup> In addition to the convective and conductive heat transfer modes, heat exchange can also occur between the continuous oil phase and water droplets if the local temperatures of the two phases are different. The third term in Eq. 1 represents the local heat exchange between the oil and water phases.

The boundary conditions associated with Eq. 1 are shown in Eq. 2

$$\left\{ \begin{array}{l} T_o = T_{o,\text{inlet}}, \text{ at } z = 0 \quad (a) \\ \frac{\partial T_o}{\partial r} = 0, \text{ at } r = 0 \quad (b) \\ U_{\text{overall}} (T_{\text{ambient}} - T_{o,\text{interface}}) = k_o \frac{\partial T_o}{\partial r}, \text{ at } r = r_{\text{interface}} \quad (c) \end{array} \right. \quad (2)$$

where

- $T_{o,\text{inlet}}(K)$  = oil temperature at the inlet
- $T_{o,\text{interface}}(K)$  = oil temperature at the interface
- $U_{\text{overall}}(W/m^2/K)$  = overall heat transfer coefficient
- $T_{\text{ambient}}(K)$  = ambient temperature
- $r_{\text{interface}}(m)$  = effective radius

For the simplicity of coding, the overall heat transfer coefficient,  $U_{\text{overall}}$ , is used in the third boundary condition, that is, boundary condition (2c), to lump the thermal resistances due to the sea water flow/coolant flow outside the pipe and the insulation by the wax deposit layer.

The governing equation and the boundary conditions for the water phase are similar to those of the oil phase but with physical properties of water, seen in Eqs. 3 and 4

water phase :

$$\rho_w C_{p_w} \phi_w V_z \frac{\partial T_w}{\partial z} + \phi_w \frac{1}{r} \frac{\partial}{\partial r} \left[ -r \left( k_w + C_{p_w} \frac{\mu_T}{Pr_T} \right) \frac{\partial T_w}{\partial r} \right] - h_{\text{inter}} (T_o - T_w) = 0 \quad (3)$$

$$\left\{ \begin{array}{l} T_w = T_{w,\text{inlet}}, \text{ at } z = 0 \quad (a) \\ \frac{\partial T_w}{\partial r} = 0, \text{ at } r = 0 \quad (b) \\ \frac{\partial T_w}{\partial r} = 0, \text{ at } r = r_{\text{interface}} \quad (c) \end{array} \right. \quad (4)$$

- $\rho_w(kg/m^3)$  = density of water
- $C_{p_w}(J/kg/K)$  = heat capacity of water
- $\phi_w$  = volume fraction of water
- $T_w(K)$  = water temperature
- $T_{w,\text{inlet}}$  = water temperature at the inlet
- $k_w(W/m/K)$  = thermal conductivity of water

Note that a zero-flux boundary condition, that is, boundary conditions (4c), is imposed on the water phase at the pipe wall. This boundary condition is used in order for the heat transfer characteristics to be consistent with the flow pattern. As the water phase is assumed to be dispersed, water droplets are not in direct contact with the wall and therefore do not conduct heat through the pipe wall.<sup>21</sup>

The governing equations are discretized and solved numerically using the numerical techniques provided by Oosthuizen and Naylor.<sup>22</sup> The two governing equations are coupled as the heat exchange terms contain both  $T_o$  and  $T_w$ . Consequently, iterations are necessary to solve for  $T_o$  and  $T_w$  simultaneously, causing the E-E approach to be more computationally intensive than the PSP approach.

*Modeling the Heat Exchange between Oil and Water Phases.* It should be noted that the heat transfer model is not completed at this point as the calculation of heat transfer coefficient between the oil and water phases,  $h_{\text{inter}}$ , has not been specified. The interphase heat transfer coefficient,  $h_{\text{inter}}$ , between the continuous oil phase and the dispersed water phase with a volume fraction of  $\phi_w$  and uniform droplet diameter of  $d_w$  can be calculated using Eq. 5.<sup>23–26</sup>

$$h_{\text{inter}} = \frac{12k_o \phi_w}{d_w^2} \quad (5)$$

$d_w(m)$  = droplet diameter

As can be seen from Eqs. 5,  $h_{\text{inter}}$  scales with  $d_w^{-2}$ . When the dispersed water droplets have a size distribution specified by the probability density function,  $P(d_w)$ , for the droplet diameter  $d_w$ , the heat transfer coefficient between two phases can be calculated by the integral shown in Eq. 6

$$h_{\text{inter}} = 12k_o \phi_w \frac{\int_0^{\infty} d_w P(d_w) dd_w}{\int_0^{\infty} d_w^3 P(d_w) dd_w} \quad (6)$$

The derivations of Eqs. 5 and 6 are included in Supporting Information Appendix B. As can be seen from Eqs. 5 and 6,

inputting an accurate droplet size distribution is essential to accurately modeling the interphase heat transfer. The droplet size distribution thus becomes an additional input parameter required for water-in-oil two phase wax deposition modeling when compared to single phase wax deposition modeling. Pulsed-NMR techniques<sup>20</sup> or microscopy experiments<sup>27</sup> can be used to measure the water droplet size distribution. When experimental characterization is not feasible, the droplet size can be estimated based on dimensional analysis reported in the studies by Grace,<sup>28</sup> Hinze et al.,<sup>29</sup> Baruner et al.,<sup>30</sup> or Cai et al.<sup>31</sup> Unfortunately, using the methods in these studies, one can only determine the upper and lower limits of the droplet diameter while the entire droplet size distribution cannot be predicted. A sensitivity analysis on the droplet diameter should then be performed to estimate the uncertainties in the deposit thickness due to the varying droplet diameter.

### Pseudosingle phase (PSP) approach

The pseudosingle phase (PSP) approach treats the water-in-oil dispersion as a single pseudofluid whose physical properties are calculated by averaging the corresponding physical properties of oil and water, as given in Eqs. 7 to 9

$$\text{density : } \bar{\rho}_{\text{mix}} = \rho_o \phi_o + \rho_w \phi_w \quad (7)$$

$$\text{heat capacity : } \bar{C}_{P_{\text{mix}}} = \frac{\rho_o \phi_o C_{P_o} + \rho_w \phi_w C_{P_w}}{\rho_o \phi_o + \rho_w \phi_w} \quad (8)$$

$$\text{thermal conductivity : } \bar{k}_{\text{mix}} = \frac{k_w + 2k_o + 2\phi_w(k_w - k_o)}{k_w + 2k_o - \phi_w(k_w - k_o)} k_o \quad (9)$$

$\bar{\rho}_{\text{mix}} (\text{kg/m}^3)$  = average density of the oil–water mixture  
 $\bar{C}_{P_{\text{mix}}} (\text{J/kg/K})$  = average heat capacity of the oil–water mixture  
 $\bar{k}_{\text{mix}} (\text{W/m/K})$  = average thermal conductivity of the oil–water mixture

The density of the pseudofluid is calculated by volume-based averaging. The heat capacity is calculated by weight-based averaging. The thermal conductivity is calculated using Maxwell's correlation.<sup>32</sup> These averaged physical properties are then used in the heat transfer governing equation and the corresponding boundary conditions, as shown in Eqs. 10 and 11

$$\text{pseudosingle phase : } \bar{\rho}_{\text{mix}} \bar{C}_{P_{\text{mix}}} V_z \frac{\partial T}{\partial z} + \frac{1}{r} \frac{\partial}{\partial r} \left[ -r \left( \bar{k}_{\text{mix}} + \bar{C}_{P_{\text{mix}}} \frac{\mu_T}{\text{Pr}_T} \right) \frac{\partial T}{\partial r} \right] = 0 \quad (10)$$

$$\left\{ \begin{array}{l} T = T_{\text{inlet}}, \text{ at } z = 0 \quad (a) \\ \frac{\partial T}{\partial r} = 0, \text{ at } r = 0 \quad (b) \\ U_{\text{overall}}(T_{\text{ambient}} - T_{\text{interface}}) = \bar{k}_{\text{mix}} \frac{\partial T}{\partial r}, \text{ at } r = r_{\text{interface}} \quad (c) \end{array} \right. \quad (11)$$

By lumping of the oil and water phases into one pseudofluid, only one temperature variable,  $T$ , is needed to describe the temperature distributions in both phases, which intrinsically assumes that the interphase heat exchange between oil and water is instantaneous. It should be noted that under certain conditions, the PSP approach becomes superior to the E-E approach due to its computational efficiency. For example, when the droplet size is fine, a large interfacial area is

available for interphase heat transfer, resulting in rapid heat transfer between the oil and water phases. The predictions from the PSP approach are then consistent with those from the E-E approach. In the next subsection, the applicability of the E-E and PSP approaches under typical field and lab conditions will be assessed to provide guidelines to select the heat transfer model for water-in-oil dispersed phase flow wax deposition modeling.

### Comparison between the PSP and E-E approach

The comparison between the PSP and E-E approach is performed based on typical parameters in a field scale pipeline as well as a lab scale flow loop. These parameters can be found in Supporting Information Appendix C.

*Field Scale Simulations.* The axial evolutions of the oil and water phase temperatures at the wall were calculated and shown in Figure 3. Note that the dimensionless oil and water phase temperatures,  $\theta_o$  and  $\theta_w$ , defined in Eq. 12, instead of the actual temperatures were plotted for a clearer comparison between the different simulations

$$\theta_o = \frac{T_o - T_{\text{ambient}}}{T_{o,\text{inlet}} - T_{\text{ambient}}}, \quad \theta_w = \frac{T_w - T_{\text{ambient}}}{T_{w,\text{inlet}} - T_{\text{ambient}}}, \quad \zeta = \frac{z}{R} \quad (12)$$

$\theta_o$  = dimensionless temperature of oil

$\theta_w$  = dimensionless temperature of water

$\zeta$  = dimensionless axial position

Figure 3 shows the axial evolutions of the dimensionless temperatures generated with a droplet diameter of (a) 1mm and (b) 1 $\mu\text{m}$ . One observes from Figure 3 that the predicted temperature profile evolutions are not sensitive to the droplet diameter. It should be noted that the external heat transfer coefficient of a field scale pipeline is usually small (on the order of 10 W/m<sup>2</sup>/K)<sup>33</sup> and as a result, the axial temperature profile evolution of the water phase will be limited by the heat loss rate to the ambient while is not limited by the heat transfer rate between oil and water even when the droplet diameter is as large as 1 mm. Under these conditions, the PSP approach will generate temperature profile predictions similar to the E-E approach for both fine droplets ( $d_w = 1\mu\text{m}$ ) and coarse droplets ( $d_w = 1\text{mm}$ ). *The take-away from this analysis is that the pseudosingle phase approach can be used for field scale simulations.*

*Lab Scale Simulations.* Unlike field operations, lab scale flow loop wax deposition experiments usually require forced convection of a coolant stream in the test section to induce wax deposition. The external heat transfer coefficient associated with this setting is usually on the order of 1 kW/m<sup>2</sup>/K.<sup>34</sup> The evolutions of the axial temperature profiles of the oil and water phases with different droplet diameters and an external heat transfer coefficient of 1 kW/m<sup>2</sup>/K are shown in Figure 4.

As can be seen from Figure 4, the droplet diameter has a significant impact on the predicted temperature profiles. *The take-away from this analysis is that when the droplet diameter is large, the temperature profile evolution is limited by the heat transfer between the oil and water phases, causing the PSP approach to break down as it cannot resolve this heat exchange.* The lab scale heat transfer model showed good performance when applied to predict the heat transfer rate in a laboratory rectangular channel.<sup>35,36</sup> Details with respect to this application of the heat transfer model is included in Appendix D.

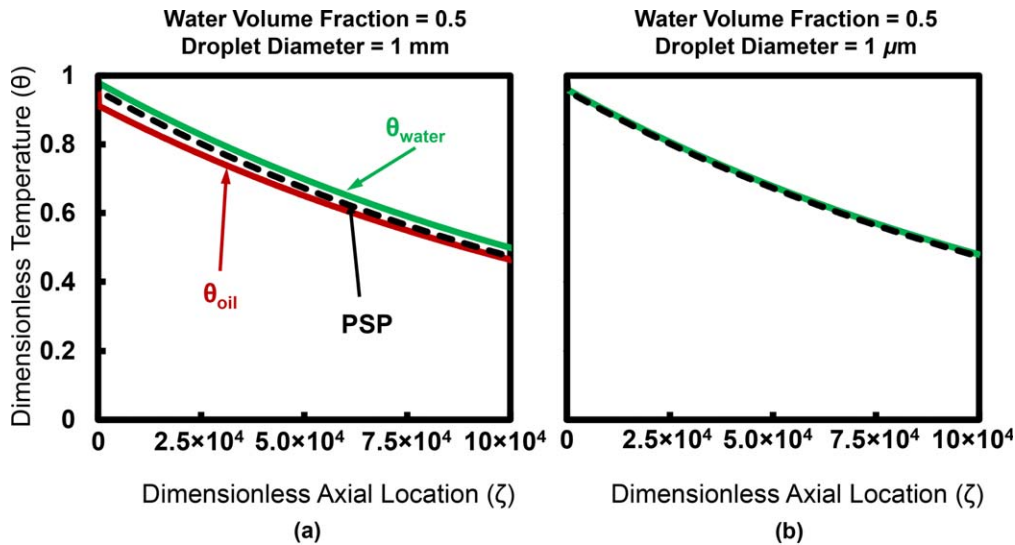


Figure 3. Dimensionless oil/water temperature profiles at wall predicted using the E-E approach and the PSP approach by assuming (a)  $d_w = 1 \text{ mm}$  and (b)  $d_w = 1 \mu\text{m}$ .

The water volume fraction in these simulations is fixed at 0.5. [Color figure can be viewed at wileyonlinelibrary.com]

*Dimensionless Analysis.* A dimensionless analysis was performed to (1) identify the dimensionless groups that govern the heat transfer characteristics, (2) explain the different heat transfer characteristics between field scale and lab scale simulations based on the different characteristic values of the dimensionless numbers encountered in these simulations and (3) propose reliable rules of thumb to select a more appropriate heat transfer approach between the PSP and E-E approaches.

Dedimensionalization of the heat transfer governing equations and boundary conditions was performed using the following definitions for dimensionless variables

$$\lambda = \frac{V_z}{U}, \quad \zeta = \frac{z}{R}, \quad \xi = \frac{r}{R}, \quad \theta_o = \frac{T_o - T_{\text{ambient}}}{T_{o,\text{inlet}} - T_{\text{ambient}}}, \quad (13)$$

$$\theta_w = \frac{T_w - T_{\text{ambient}}}{T_{w,\text{inlet}} - T_{\text{ambient}}}$$

The dimensionless form of the oil phase heat transfer equation is shown in Eq. 14.

$$\phi_o \lambda \frac{\partial \theta_o}{\partial \zeta} + \phi_o \frac{1}{\xi} \frac{\partial}{\partial \xi} \left( -\frac{1}{\text{Pe}_R} \xi \frac{\partial \theta_o}{\partial \xi} \right) - \text{St}_R (\theta_o - \theta_w) = 0 \quad (14)$$

Two dimensionless numbers, that is, the Péclet number,  $\text{Pe}_R$  and the Stanton number,  $\text{St}_R$ , surfaced through the dedimensionalization of Eq. 1 and are given in Eqs. 15 and 16, respectively

$$\text{Pe}_R = \frac{UR}{(\varepsilon_o + \alpha_o)} \quad (15)$$

with  $\varepsilon_o = 0$  for laminar flow,  $\varepsilon_o > 0$  for turbulent flow

$$\text{St}_R = \frac{h_{\text{inter}} R}{\rho_o C_{p_o} U} \quad (16)$$

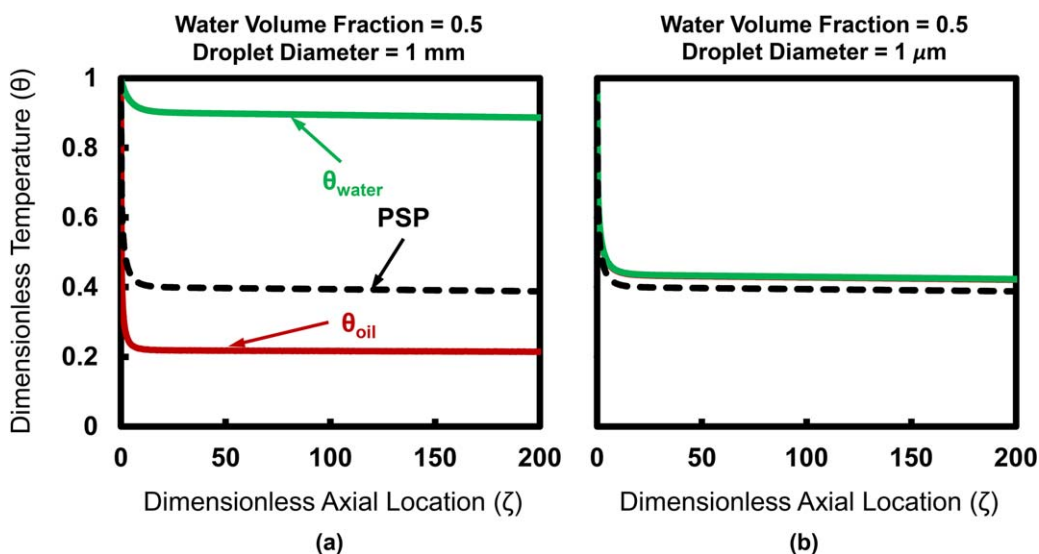


Figure 4. Dimensionless oil/water temperature profiles at wall predicted using the E-E approach and the PSP approach by assuming (a)  $d_w = 1 \text{ mm}$  and (b)  $d_w = 1 \mu\text{m}$ .

The water volume fraction in these simulations is fixed at 0.5. [Color figure can be viewed at wileyonlinelibrary.com]

The subscript “*R*” in the definitions for the Péclet and Stanton numbers represents that the radius of the pipe is used as the characteristic length scale. The dimensionless boundary conditions are shown in Eq. 17

$$\text{Nu}\theta_o + \frac{d\theta_o}{d\xi} = 0, \text{ at } \xi = 1$$

$$\text{Nu}_R = \frac{U_{\text{overall}}R}{k_o} \quad (17)$$

The boundary conditions have been given in dimensionless form with the external heat transfer coefficient, thermal conductivity of the oil and pipe radius grouped in the Nusselt number  $\text{Nu}_R$ . Among the three dimensionless numbers,  $\text{St}_R$  and  $\text{Nu}_R$  directly affect the heat transfer characteristics.  $\text{St}_R$  characterizes the rate of heat exchange between the oil phase and the water droplets phase while  $\text{Nu}_R$  characterizes the rate of heat loss from the oil phase to the coolant stream or the surrounding sea water through the pipe wall. To present the roles of  $\text{St}_R$  and  $\text{Nu}_R$  on the temperature profile predictions, the dimensionless governing equations and boundary conditions were solved with various combinations of these two parameters, that is, different pairs of  $(\text{St}_R, \text{Nu}_R)$ . The maximal differences between the dimensionless oil and water temperatures,  $\Delta\theta_{\text{max}} = (\theta_w - \theta_o)$ , generated with different pairs of  $(\text{St}_R, \text{Nu}_R)$  were shown in Figure 5.  $\Delta\theta_{\text{max}}$  is an efficient indicator for the validity of the PSP model. A large  $\Delta\theta_{\text{max}}$  suggests that the PSP model is invalid as it cannot resolve this difference between the oil and water phase temperatures.

In Figure 5, a difference between the dimensionless water and oil temperatures of 0.5, that is,  $\Delta\theta_{\text{max}} = 0.5$  represents that the maximal difference between the water and oil phase interface temperatures among all axial positions is 50% that of the difference between the inlet temperature and the ambient/coolant temperature. As can be seen from Figure 5, the effect of droplet size on heat transfer becomes less profound as  $\text{Nu}_R$  decreases because at low values of  $\text{Nu}_R$ , the temperature profile evolution is no longer limited by the heat transfer rate between oil and water but limited by the heat loss rate to the coolant stream/surrounding sea water. Such heat transfer characteristics at low  $\text{Nu}_R$  can usually be encountered with small external heat transfer coefficients such as the ones used in the field scale. As can be seen in Figure 5, the PSP approach is likely to breakdown at high  $\text{Nu}_R$  and low  $\text{St}_R$  conditions, which can be encountered with intensive cooling by the

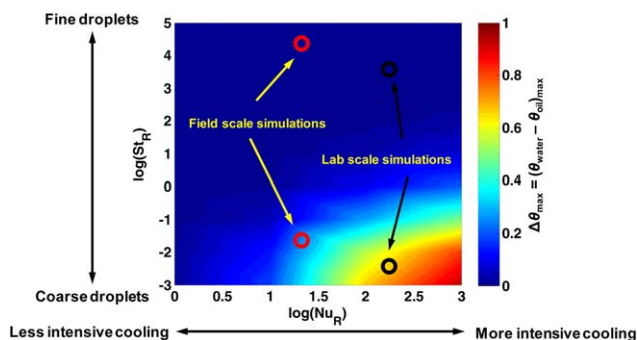


**Figure 5.** Assessment of the applicability of the pseudo-single phase (PSP) approach for heat transfer calculation under various  $(\text{St}_R, \text{Nu}_R)$  conditions.

[Color figure can be viewed at wileyonlinelibrary.com]

**Table 1. Recommended Selection for Heat Transfer Model based on the Characteristic Dimensionless Numbers,  $\text{Nu}_R$  and  $\text{St}_R$**

	Field Scale Cooling ( $\text{Nu}_R \sim 10^1$ )	Lab Scale Cooling ( $\text{Nu}_R \sim 10^2$ )
Coarse droplet diameter ( $\text{St}_R < 10^{-1}$ )	PSP	E-E
Fine droplet diameter ( $\text{St}_R > 10^0$ )	PSP	PSP

ambient/coolant in lab scale simulations. Table 1 provides some quantitative rules of thumb to select the appropriate heat transfer approach depending on the magnitude of dimensionless numbers.

### Mass Transfer Calculations

It is accepted that molecular diffusion is the main mechanism responsible for wax deposition.<sup>1–10</sup> To calculate the radial diffusive flux of wax molecules and the deposit growth rate, the concentration profile of dissolved wax in the oil phase needs to be determined by solving the mass transfer governing equation, that is, Eq. 18

$$V_z \frac{\partial C_{\text{wax}}}{\partial z} + \frac{1}{r} \frac{\partial}{\partial r} \left[ -r(\varepsilon_M + D_{\text{wo}}) \frac{\partial C_{\text{wax}}}{\partial r} \right] + k_{\text{precipitation}}(C_{\text{wax}} - C_{\text{wax},\text{eq}}) = 0 \quad (18)$$

where

$C_{\text{wax}}$  ( $\text{kg}/\text{m}^3$ ) = concentration of wax in the liquid phase

$C_{\text{wax},\text{eq}}$  ( $\text{kg}/\text{m}^3$ ) = equilibrium concentration of wax at local temperature

$D_{\text{wo}}$  ( $\text{m}^2/\text{s}$ ) = molecular diffusivity of wax in oil

$\varepsilon_M$  ( $\text{m}^2/\text{s}$ ) = effective diffusivity of wax in oil

$k_{\text{precipitation}}$  ( $\text{s}^{-1}$ ) = bulk precipitation kinetic constant

The boundary conditions to Eq. 18 are

$$\begin{cases} C_{\text{wax}} = C_{\text{wax},\text{inlet}}, \text{ at } z = 0 & (a) \\ \frac{\partial C_{\text{wax}}}{\partial r} = 0, \text{ at } r = 0 & (b) \\ C_{\text{wax}} = C_{\text{wax},\text{eq},\text{interface}}(T_{\text{interface}}), \text{ at } r = r_{\text{interface}} & (c) \end{cases} \quad (19)$$

The bulk precipitation kinetic constant,  $k_{\text{precipitation}}$ , cannot be easily characterized in a flowing system such as in a field pipeline or a laboratory flow loop. Consequently, wax deposition simulations are usually performed by assuming one of the two limiting situations:

- no precipitation of wax in the bulk ( $k_{\text{precipitation}} = 0$ ), also known as the Chilton–Colburn method<sup>1</sup>
- instantaneous precipitation of wax in the bulk ( $k_{\text{precipitation}} \rightarrow \infty$  and  $C_{\text{wax}} \rightarrow C_{\text{wax},\text{eq}}$ ), also known as the solubility method<sup>37</sup>

These two simulations are expected to provide reliable estimations for the most conservative (the largest deposit) and optimistic (the smallest deposit) estimations of deposit thickness, respectively. Two methods to calculate the diffusivity of wax were proposed for these two limiting cases for bulk precipitation kinetics. These two methods will be explained in detail in the subsections to follow.

### The Chilton–Colburn method

It should be noted that in water-in-oil dispersed phase flows, diffusion of wax can only occur in the oil continuous phase as the wax molecules are insoluble in water droplets. In order to incorporate this mass transfer characteristic, the following boundary condition needs to be imposed on the oil-water interfaces of *each and every* water droplet

$$\vec{n} \cdot \vec{J}_{\text{wax}} = \vec{n} \cdot \left( -D_{\text{wo}} \vec{\nabla} C_{\text{wax}} \right) = 0, \text{ on oil-water interfaces} \quad (20)$$

$\vec{n}$  = the local normal vector to the oil–water interface

$\vec{J}_{\text{wax}}$  (kg/m<sup>2</sup>/s) = the diffusive flux of wax in oil

The governing equation and the boundary conditions shown in Eqs. 18–20 appear to be mathematically simple and one might be tempted to solve this system using conventional computational fluid dynamics (CFD) techniques. However, before going down this path, we first need to estimate the computational intensity of a conventional CFD model by estimating the number of cells in the computational domain of the entire pipe. We will perform this estimation by considering a 1-km, 12-in. (0.305 m) pipe section filled with a water-in-oil dispersion at a water volume fraction of 0.1. If the droplets have a uniform diameter of 10 microns, we can calculate that this imaginary pipe section contains as many as 10<sup>15</sup> water droplets. To resolve the diffusion of wax molecules around the water droplets, the computational cells in the vicinity of the droplet-oil interfaces should be finer in size than the water droplets, resulting in even more than 10<sup>15</sup> computational cells to be constructed for the entire computational domain. Such computational intensity forbids “naïve” CFD simulations without any “tailor-made” modifications. Strategies to reduce computational intensity were developed in this study and will now be presented in the upcoming subsections.

**Approach I—Method of Volume Averaging.** To reduce computational intensity, the method of volume averaging technique uses effective transport properties to account for the impact of transport barriers, such as water droplets. It should be emphasized that the method of volume averaging is applicable when the droplet diameter (e.g., ~1 μm) is significantly smaller than the mass transfer boundary layer thickness (e.g., ~100 μm). Under this condition, the boundary layer contains a sufficient number of droplets and has a homogeneous microstructure, which guarantees that volume averaging can generate representative effective transport properties.

One can account for the partially blocked wax diffusion by using  $D_{\text{eff}}$  in place of  $D_{\text{wo}}$  in the governing equation. The effective diffusivity in dispersion can be predicted with the method of volume averaging by first solving the mass balance in a control volume with a sufficient number of water droplets and the integrated volume-averaged flux can then be compared with the flux in absence of droplets, shown in Eq. 21.

$$\frac{D_{\text{eff}}}{D_{\text{wo}}} = \frac{J_{\text{wax}}}{J_{\text{wax, single}}} = \frac{\frac{1}{V_{\text{oil}}} \iiint_{V_{\text{oil}}} -D_{\text{wo}} \nabla C_{\text{wax}} dV_{\text{oil}}}{J_{\text{wax, single}}} \quad (21)$$

$D_{\text{eff}}$  (m<sup>2</sup>/s) = Effective diffusivity of wax in the water-oil mixture

$J_{\text{wax}}$  (kg/m<sup>2</sup>/s) = Diffusive flux of wax in the direction of the macroscopic concentration gradient in water-oil mixture

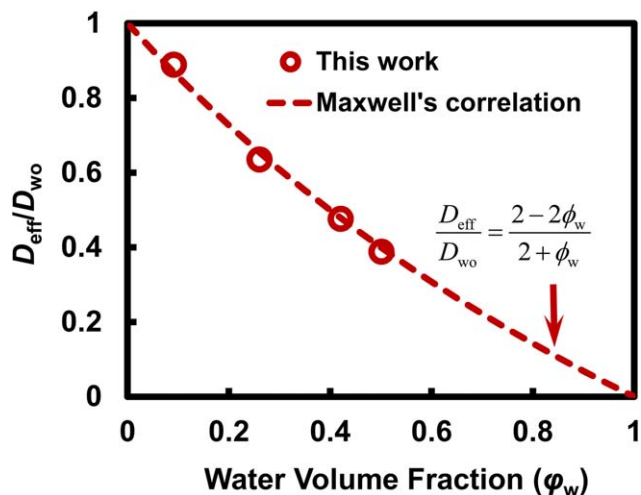


**Figure 6.** Comparison between the effective diffusivities estimated by the microscopic model and theoretical values by Maxwell–Garnett correlation.

[Color figure can be viewed at [wileyonlinelibrary.com](http://wileyonlinelibrary.com)]

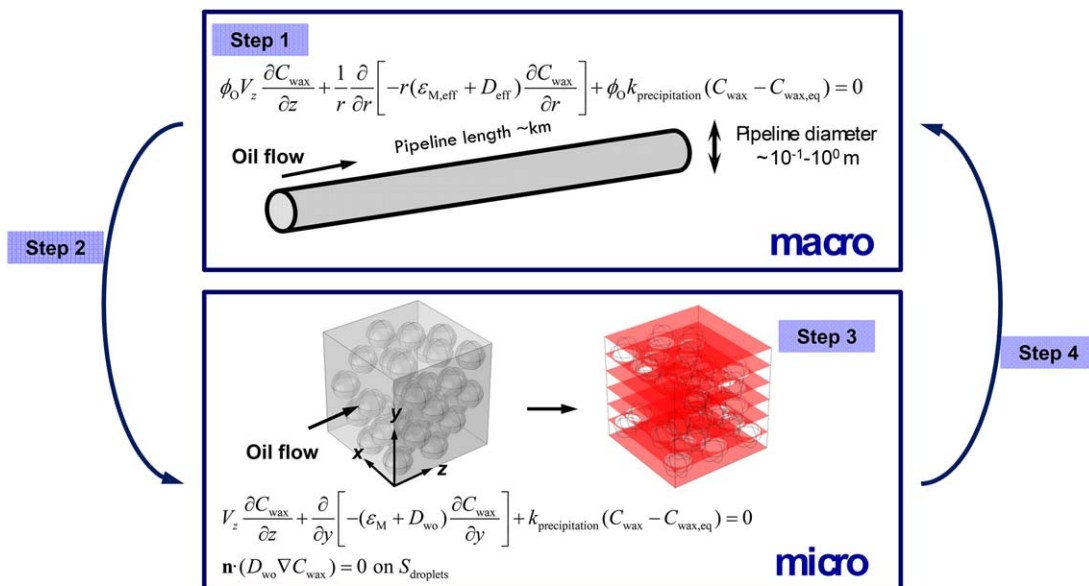
$J_{\text{wax, single}}$  (kg/m<sup>2</sup>/s) = Diffusive flux of wax in the direction of the macroscopic concentration gradient in single phase oil

$V_{\text{oil}}$  (m<sup>3</sup>) = Volume of the continuous oil phase in the control volume

The predicted effective diffusivities by CFD are compared with the predictions by the Maxwell–Garnett equation in Figure 6. Other computational details regarding the CFD model can be found in Supporting Information Appendix E.

As can be seen from Figure 6, excellent agreement is achieved between  $D_{\text{eff}}/D_{\text{wo}}$  predicted by the Maxwell–Garnett equation and by the CFD model and thereby validating the CFD model. The variation of the effective diffusivity with water volume fraction is also consistent with the effect of water volume fraction on the tortuosity of the continuous oil phase measured by NMR.<sup>27</sup>

**Approach II—Method of Ensemble Averaging.** The method of volume averaging fails when the droplet size is comparable to or larger than the boundary layer thickness. When the droplet diameter is larger than the mass transfer boundary layer thickness, droplets will not fit into the mass transfer boundary layer. Consequently, the mass transfer boundary layer has a lower water volume fraction than the bulk. The volume fraction of the entire flow is thus not representative of the water volume fraction of the boundary layer. Under this circumstance, a novel method, the method of ensemble averaging is proposed to model the mass transfer around droplets. This method of ensemble averaging is initiated by solving the mass transfer equation at the pipeline scale by assuming  $D_{\text{eff}} = D_{\text{wo}}$  as an initial guess, shown as “Step-1” in Figure 7. The preliminary concentration profiles obtained by the macroscopic simulation are then used as the boundary conditions for a microscopic CFD simulation performed at a region in the immediate vicinity of the pipe wall, shown as “Step-2” in Figure 7. A series of cut planes are then constructed in parallel with the wall and the diffusive mass transfer rates across each cut plane,  $\iint J_{\text{wax}} dA_{\text{cutplane}}$ , are calculated and compared to the mass transfer rate in absence of the water droplets, shown as “Step-3” in Figure 7. Based on the comparison between the calculated mass transfer rates with and



**Step 1:** Solve the macroscopic mass transfer equation with initial guesses:  $D_{eff} = D_{wo}$ ,  $\epsilon_{M,eff} = \epsilon_M$

**Step 2:** Use the concentration profiles from macroscopic simulations from step 1 as inputs to microscopic simulations as boundary conditions.

**Step 3:** Solve the microscopic mass transfer equation. A series of parallel cut-planes are then constructed and the diffusive mass transfer rate across each plane calculated based on the solution to the concentration profile.

**Step 4:** Compare the mass transfer rate across the cut-plane in presence of droplets with that in absence of droplets to calculate effective diffusivity. The effective diffusivity is then used in a second macroscopic simulation to determine mass flux of wax to the interface.

**Step 5:** Repeat Step 1 through Step 4 until the predicted macroscopic radial concentration profile does not change.

**Figure 7. The algorithm to evaluate the effective diffusivity in the vicinity of the wall when the droplet size is larger or comparable to the boundary layer thickness.**

[Color figure can be viewed at [wileyonlinelibrary.com](http://wileyonlinelibrary.com)]

without droplets, a local diffusivity reduction parameter can be defined according to Eq. 22

$$\lambda(y) = \frac{\iint J_{wax} dA_{cutplane}}{\iint J_{wax,0} dA_{cutplane,0}} = \frac{\iint D_{wo} \nabla C_{wax} dA_{cutplane}}{\iint D_{wo} \nabla C_{wax,0} dA_{cutplane,0}} \quad (22)$$

This reduction in diffusivity is then incorporated into the macroscopic modeling with the effective diffusivity, replacing the molecular diffusivity, shown as “Step-4” in Figure 7. Steps 1–4 are repeated until the predicted macroscopic concentration profile no longer changes. This converged concentration profile is then used to calculate the flux toward the wall/interface. Figure 8 shows the calculated diffusivity reduction parameter for cases with various droplet diameters.

As can be seen from Figure 8, the reduction in diffusivity at the interface/wall  $[\frac{\lambda}{a}] = 0$  becomes less significant as the droplet diameter increases. It should be noted that the droplet configurations in the control volume is generated by packing spheres into a cubic simulation box with Monte Carlo simulation.<sup>38,39</sup> Therefore, periodic oscillations in the diffusivity reduction are observed due to the oscillations in the local porosity of the sphere packing. Several microscopic configurations of the droplets were generated to form an ensemble and

the predicted diffusivity reduction was averaged over all configurations to obtain an ensemble-average of the diffusivity reduction. Details of the ensemble average method to obtain the effective diffusivity can be found in Supporting Information Appendix F.

*In summary, when the boundary layer thickness is much larger than the droplet diameter, the retarded molecular diffusion in the boundary layer due to droplets can be accounted for using the effective diffusivity calculated by the Maxwell–Garnett equation. When the boundary layer thickness is comparable or smaller than droplet diameter, the method of volume averaging overestimates the hindrance of droplets to molecular diffusion. The method of ensemble averaging is more reliable for mass transfer modeling.*

#### The solubility method

For the case of instantaneous bulk precipitation, it was discovered through CFD simulation that the concentration of dissolved wax within the oil phase is at the equilibrium concentration at local temperature and is not affected by the presence of the water droplets. Details regarding the CFD simulation were provided in Supporting Information Appendix G. As a result, mass transfer calculations are not necessary to determine the dissolved wax concentration profile for the case



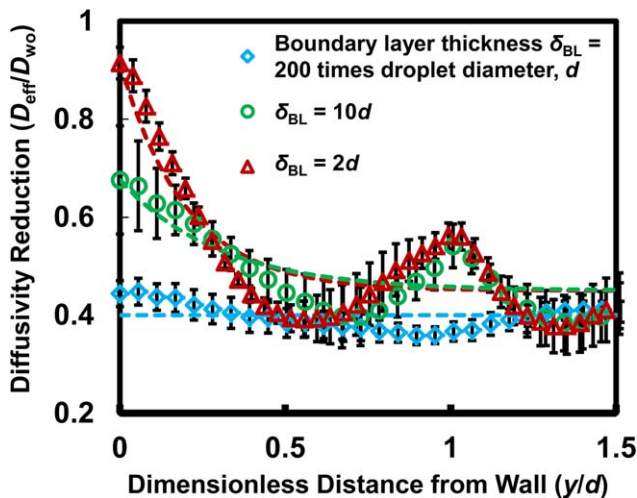


**Figure 8.** Diffusivity reduction parameter calculated with three varying droplet diameters: (1) the boundary layer thickness being 200 times the droplet diameter, (2) the boundary layer thickness being 10 times the droplet diameter and (3) the boundary layer thickness being two times the droplet diameter.

[Color figure can be viewed at [wileyonlinelibrary.com](http://wileyonlinelibrary.com)]

of instantaneous precipitation. The diffusive flux of wax reaching the oil/deposit interface (or oil/wall interface at  $t=0^+$ ) can be calculated based on the wax equilibrium concentration gradient and the molecular diffusivity at the interface, as shown in Eq. 23

$$J_{\text{wax}}|_{r=r_{\text{interface}}} = -D_{\text{wo}} \frac{\partial C_{\text{wax,eq}}}{\partial r}|_{r=r_{\text{interface}}} \quad (23)$$

$J_{\text{wax}}|_{r=r_{\text{interface}}}$  ( $\text{kg}/\text{m}^2$ ) = diffusive flux of wax to the oil/deposit interface (or oil/wall interface at  $t=0^+$ )

The calculated flux of wax can then be used to determine the deposit growth rate.

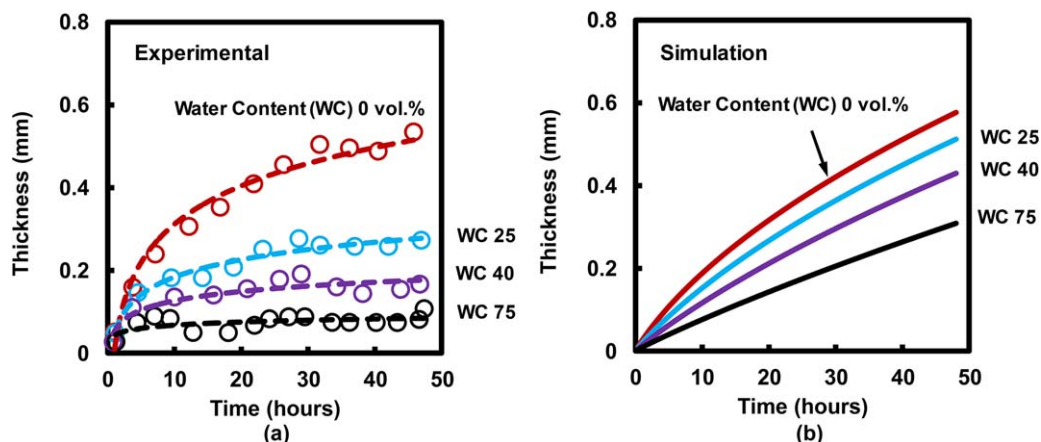


**Figure 9.** Comparison between predicted and measured deposit thickness-time trajectories with varying water volume fractions.

[Color figure can be viewed at [wileyonlinelibrary.com](http://wileyonlinelibrary.com)]

## Application of the Algorithm in Wax Deposition Modeling

### Case study 1: Wax deposition in a lab scale flow loop apparatus

Although multiple experimental studies<sup>18,36,40</sup> have showed that wax deposit thickness tends to decrease with increasing water volume fraction, a detail theoretical analysis of this experimental observation is lacking. In this section, a theoretical analysis is performed to understand the role of the water phase on the deposit thickness from fundamentals of heat and mass transfer. The input parameters for simulation are based on the conditions of the flow loop experiments by Bruno et al.<sup>18</sup> These input parameters were summarized in Supporting Information Appendix H. The water volume fraction of the simulation is varied from 0% to as high as 75%. The solubility method, that is, instantaneous bulk precipitation kinetics, is used for this set of simulations. The comparison between the deposit thickness predictions and the experimentally measured thickness is shown in Figure 9.

As can be seen from Figure 9, the model predicts the experimental trend of decreasing deposit thickness as a function of increasing water volume fraction, which serves as a first validation of the model. It can also be observed from the experimental thickness-time trajectories that the deposit thickness decreases with time on several occasions, suggesting slough-off of deposit by the shear force. The slough-off of deposit is random and cannot be accounted for in wax deposition modeling. Now, we will analyze the trend of decreasing deposit thickness with increasing water volume fraction based on heat and mass transfer analysis. The thickness of wax deposit can be correlated with the mass flux of wax reaching the interface, shown in Eq. 24

$$\text{growth rate } \frac{d\delta}{dt} \sim J_{\text{wax}} = -D_{\text{wo}} \frac{\partial C_{\text{wax}}}{\partial r}|_{\text{wall}} \sim D_{\text{wo}} \frac{C_{\text{bulk}} - C_{\text{wall}}}{\delta_{\text{BL}}} \quad (24)$$

The water phase can affect the concentration driving force,  $(C_{\text{bulk}} - C_{\text{wall}})$  and the boundary layer thickness  $\delta_{\text{BL}}$ . The effect of water volume fraction on the boundary layer thickness is first investigated by inspecting the radial dissolved wax concentration profiles predicted with different water volume

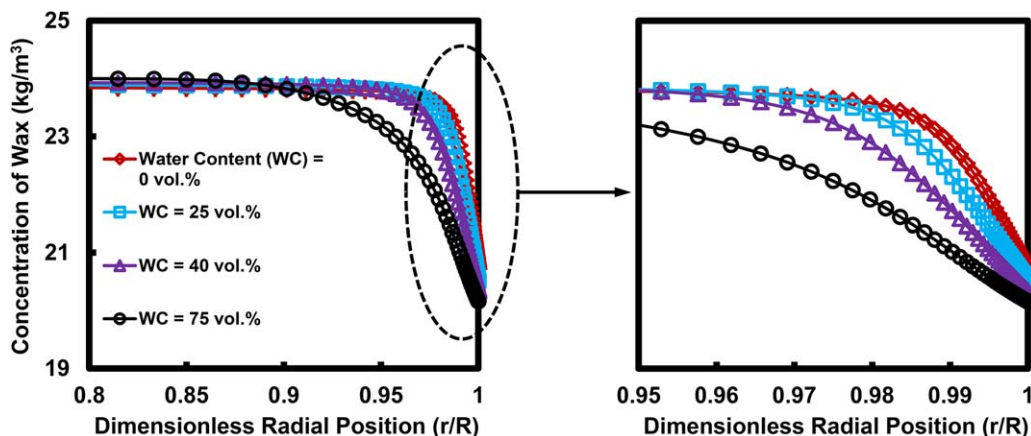


Figure 10. Predicted radial concentration profiles of dissolved wax with varying water volume fractions.

[Color figure can be viewed at [wileyonlinelibrary.com](http://wileyonlinelibrary.com)]

fractions. As can be seen from the predicted radial concentration profiles of dissolved wax shown in Figure 10, the concentration boundary layer thickness increases with increasing water volume fraction due to the increase in viscosity of the water–oil mixture, leading to a decrease in the concentration gradient of wax and deposition rate.

Now, let us consider the effect of the water phase on the concentration driving force for wax deposition,  $(C_{\text{bulk}} - C_{\text{wall}})$ , which depends on the concentrations of wax dissolved in the bulk and at the wall,  $C_{\text{bulk}}$  and  $C_{\text{wall}}$ , respectively. Due to the short length of the experimental test section, the bulk temperature remains almost unchanged across the test section, as evidenced by the fact that the bulk temperature at the outlet remained within  $1^{\circ}\text{C}$  from the inlet temperature. The wall temperature is also insensitive to the water volume fraction. The oil temperature at the interface varied between  $12.6^{\circ}\text{C}$  and  $10.5^{\circ}\text{C}$  when the water volume fraction was varied between 0 and 75 vol %. It should be noted that the oil temperature at the interface is close to the coolant temperature due to the large external heat transfer coefficient,  $h_{\text{ext}}$ . Because of the negligible changes in the bulk and interface temperatures with varying water volume fraction, the concentration driving force is also insensitive to the water volume fraction. *The decreased deposit thickness with increasing water volume fraction is explained by the retarded heat transfer due to the increase in viscosity when there are water droplets dispersed in oil.*

### Case study 2: Field scale wax deposition predictions

The goal of this model development is to predict wax deposition rates in field scale oil pipelines. Therefore, it is desirable to bench-mark our model with wax deposition data from actual subsea pipelines. Unfortunately, no such wax deposition data is available in the public domain. The performance of this model will be evaluated by simulating wax deposition under the field scale operating conditions included in Supporting Information Appendix I. The wax solubility and viscosity curves used in this case study are identical to those used in the previous lab scale case study.

The water volume fraction in the feed is varied from 0 to 50 vol %. Figure 11 shows the predicted deposit thickness.

Two observations can be made from Figure 11. First, the water phase significantly delays the onset of wax deposition and second, local deposit thickness increases with increasing water volume fraction. These two observations will now be

explained separately. As the water volume fraction of the feed varies from 0 to 50 vol.%, the onset location of wax deposition is shifted downstream by almost 10 km. This observation can be explained by the change in the oil temperature at wall with varying water volume fraction. Figure 12 shows the predicted wall temperature at different water volume fractions.

As can be seen from Figure 12, the wall temperature in the axial direction decreases at a slower rate with an increased water volume fraction in the feed. Hence, the water phase acts as a heat carrier and retards the decrease of wall temperature with axial position. Therefore, the wall temperature reaches the wax appearance temperature at an axial location further from the entrance, thus shifting the onset of wax deposition toward downstream.

In addition to the delay in the onset of wax deposition, the local deposit thickness increases with the increasing water volume fraction. This trend at first appears to be counter-intuitive! The increase in deposit thickness with increasing water volume fraction can be explained by inspecting the heat flux from the oil to the ambient surroundings. The correlation between the deposition rate and the heat flux can be established via the following derivation shown in Eq. 25

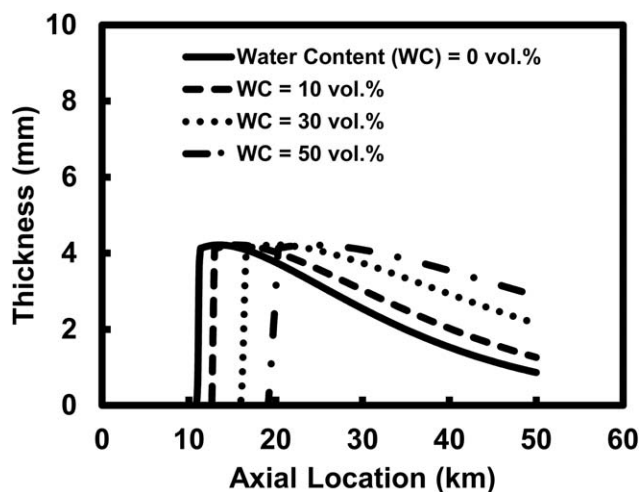


Figure 11. Predictions of axial deposit thicknesses in a field pipeline with varying water volume fractions in the feed.

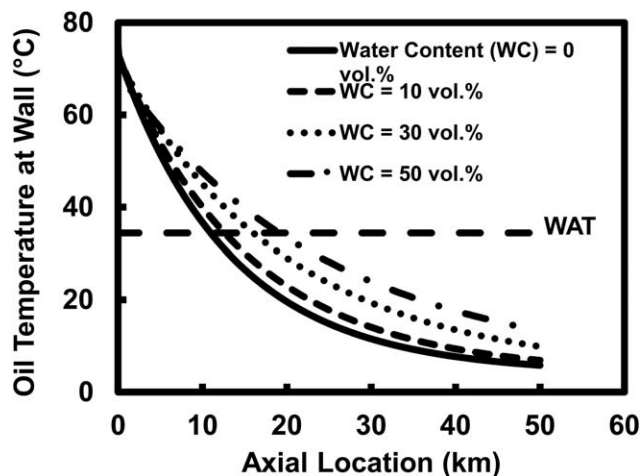


Figure 12. Axial oil temperature at wall with varying water volume fractions.

$$\begin{aligned} \text{growth rate} : \frac{d\delta}{dt} &\sim J_{\text{wax}} = -D_{\text{wo}} \left. \frac{\partial C_{\text{wax}}}{\partial r} \right|_{\text{wall}} \\ J_{\text{wax}} &= -D_{\text{wo}} \left. \frac{dC_{\text{wax}}}{dT} \right|_{T_{\text{wall}}} \cdot \left. \frac{\partial T}{\partial r} \right|_{\text{wall}} \\ (\text{valid with instantaneous bulk precipitation}) \\ &= -D_{\text{wo}} \left. \frac{dC_{\text{wax}}}{dT} \right|_{T_{\text{wall}}} \cdot k_{\text{oil}} \left. \frac{\partial T}{\partial r} \right|_{\text{wall}} \cdot \frac{1}{k_{\text{oil}}} \\ &= D_{\text{wo}} \left. \frac{dC_{\text{wax}}}{dT} \right|_{T_{\text{wall}}} \cdot h_{\text{extn}} (T_{\text{wall}} - T_{\text{ambient}}) \frac{1}{k_{\text{oil}}} \\ &= D_{\text{wo}} \left. \frac{dC_{\text{wax}}}{dT} \right|_{T_{\text{wall}}} \cdot \frac{1}{k_{\text{oil}}} \cdot Q_{\text{oil to ambient}} \end{aligned} \quad (25)$$

As can be seen from Eq. 25, the deposition rate increases with increasing heat flux from the oil to the surrounding sea water,  $Q_{\text{oil to ambient}}$ . As the wall temperature,  $T_{\text{wall}}$ , increases with increasing water volume fraction, so does the heat flux to the surrounding sea water:  $\{Q_{\text{oil to ambient}} [= h_{\text{extn}} (T_{\text{wall}} - T_{\text{ambient}})]\}$ . Thus, the local deposition rate increases with water volume fraction. It should be noted that the deposit thickness decreases with increasing water volume fraction in the lab scale simulation while the deposit thickness increases with increasing water volume fraction in this field scale simulation. The opposite trends of the deposit thickness as a function of water volume fraction will now be analyzed.

In lab scale simulations, a large external heat transfer coefficient (on the order of  $1 \text{ kW/m}^2/\text{K}$ ) is used to represent the intensive cooling by forced convection of a coolant stream around the hot oil flow. The thermal resistance of the oil flow is larger than the thermal resistance of the coolant stream. Consequently, the overall thermal resistance to heat loss from the oil to the coolant is dominated by the thermal resistance of the oil flow. As a result, the increase in the viscosity of the oil–water flow with increasing water volume fraction causes a corresponding increase in the overall thermal resistance and retards the heat loss, leading to a decrease in deposition rate in lab scale simulations. In a field scale simulation, a small external heat transfer coefficient (on the order of  $0.01 \text{ kW/m}^2/\text{K}$ ) is used to represent the cooling by sea water. As a result, the overall thermal resistance of heat loss from a field scale pipeline is dominated by the thermal resistance of

the surrounding sea water and the increase in the fluid viscosity by water does not impact heat transfer significantly. Conversely, the water phase generates a large temperature driving force for heat transfer by raising the interface temperature due to the high heat capacity of the water. This increase leads to a higher heat loss rate and therefore higher deposition rate at higher water volume fraction in field scale simulations. The opposite trends in the deposit thickness with varying water volume fraction predicted with lab scale and field scale simulations challenge the relevance of lab scale experiments on water-in-oil dispersed phase flow performed previously.<sup>18,36</sup>

### Case study 3: The effect of droplet size on wax deposition

It should be noted that no investigation, theoretical or experimental, has been performed to understand the effect of droplet size on wax deposition rate owing to the lack of a fundamental wax deposition model. Previous elementary modeling studies consider the water and oil mixture as one pseudofluid and, therefore, cannot resolve the effect of droplet size on wax deposition. To provide insights to the effect of droplet size on wax deposition rate, we now perform two wax deposition simulations by assuming a droplet diameter of  $1 \text{ mm}$  and  $1 \mu\text{m}$ , respectively. The Chilton–Colburn approach was used for the bulk precipitation kinetics. The pipe dimensions, operating conditions and fluid properties were summarized in Supporting Information Appendix J. Figure 13 shows the comparison between the wax deposition rates predicted with the two different assumed droplet sizes.

Two observations can be made from Figure 13

- The plateau of the wax deposit thickness predicted with a droplet diameter of  $1 \text{ mm}$  is higher than that predicted with a droplet diameter of  $1 \mu\text{m}$ .
- The rate that the thickness approaches the plateau value is higher for droplet diameter of  $1 \text{ mm}$  compare to that of a droplet diameter of  $1 \mu\text{m}$ .

These two observations are due to the different roles of droplet size on heat and mass transfer, respectively. First, the

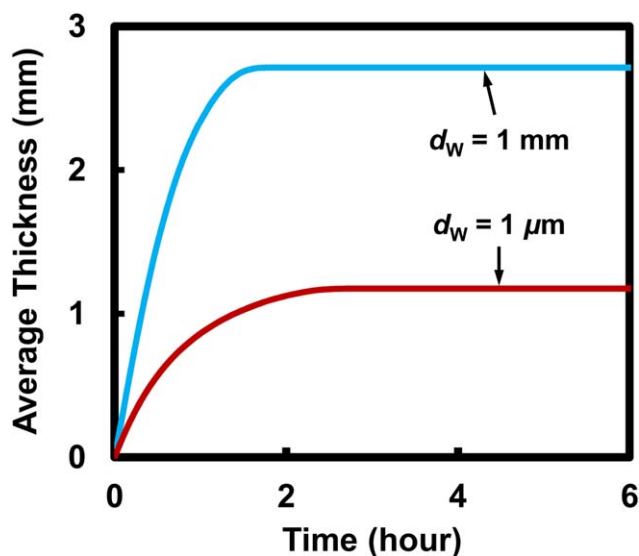


Figure 13. Comparison between deposit thickness predictions generated with an assumed droplet diameter of  $1 \text{ mm}$  and an assumed droplet diameter of  $1 \mu\text{m}$ .

[Color figure can be viewed at [wileyonlinelibrary.com](http://wileyonlinelibrary.com)]

**Table 2. Comparison of the Parameters for the Characteristic Mass Fluxes Associated with different Assumed Droplet Diameters**

	$d = 1\mu\text{m}$	$d = 1\text{ mm}$
$T_{\text{oil}}$ (°C)	45	45
$T_{\text{wall}}$ (°C)	18	12
$(C_{\text{bulk}} - C_{\text{wall}})$ (wt %)	4.86	5.13
$D_{\text{eff}}$ ( $\times 10^{-10}$ m <sup>2</sup> /s)	0.27	0.49
$J_{\text{wax}}$ ( $\times 10^{-10}$ wt %/m <sup>2</sup> /s)	260	490

thickness reaches a plateau value when the interface temperature reaches the WAT due to the insulation provided by the deposit layer. As the droplet size decreases, it is easier for water to supply heat to the oil phase and raise the oil-phase temperature. As a result, at smaller droplet sizes, the interface temperature reaches the WAT more rapidly and with a thinner deposit layer. The reduced deposition rate with decreasing water droplet size can be understood by inspecting the characteristics wax flux generated with different water droplet diameter. The definition of the characteristic wax flux was first proposed by Huang et al. to explain the effect of operating temperature on wax deposition.<sup>8</sup> Equation 26 gives the wax flux used in this investigation

$$J_{\text{wax}} = D_{\text{eff}} \left( \frac{C_{\text{bulk}} - C_{\text{wall}}}{r_{\text{interface}}} \right) \quad (26)$$

Note that the molecular diffusivity of wax,  $D_{\text{wo}}$ , in Huang et al.'s original definition is replaced with the effective diffusivity,  $D_{\text{eff}}$ , to account for the hindered diffusion of wax due to dispersion of water droplets. Table 2 summarizes the important parameters in the calculation of the characteristic wax flux.

As can be seen from Table 2, the concentration driving forces,  $(C_{\text{bulk}} - C_{\text{wall}})$ , predicted with different droplet diameters are virtually the same, while the effective diffusivity increases by a factor of approximately two when the droplet diameter increases from 1 micron to 1 millimeter. This impact of the change in effective diffusivity on wax deposition rate has not been previously investigated or reported in literature. Another simulation was performed with a droplet diameter at 1 millimeter and the method of volume averaging for the diffusivity calculation. It was observed that the initial deposition rate varies from 3.0 to 1.8 mm/h when the method of volume averaging is used. It should be noted that this ~40% underprediction is sometimes acceptable when generating a first estimation of the wax deposition rate during the design phase of field development. The method of ensemble averaging is of better physical basis while the method of volume averaging can also be used for engineering applications as a first estimation.

## Conclusions

In this study, a wax deposition model in water-in-oil dispersed flows was developed. Two approaches for heat transfer calculations, that is, the pseudosingle phase approach (PSP) and the Eulerian–Eulerian approach (E-E), are introduced and compared. The following characteristics were observed for the two heat transfer models:

E-E approach is suitable for cases with high external heat transfer coefficient and coarse droplets.

PSP model is suitable for cases with low external heat transfer coefficient or fine droplets.

It was pointed out that mass transfer modeling is not necessary when the solubility approach is used for bulk precipitation kinetics. When the Chilton–Colburn approach is used for the bulk precipitation kinetics, two methods for mass transfer modeling can be used depending on the relative sizes of the droplet and the mass transfer boundary layer. The following mass transfer characteristics were discovered from mass transfer analysis:

When the droplet size is much smaller than the mass transfer boundary layer, the effect of water droplets on mass transfer can be accounted for by using an effective diffusivity calculated using the Maxwell–Garnett equation.

When the droplet size is comparable/larger than the mass transfer boundary layer thickness, droplets cannot fit into the boundary layer. Therefore, the hindrance of molecular diffusion is less profound than the case with fine droplets. The effective diffusivity can be calculated by a novel method of ensemble averaging.

With these enhancements in the heat and mass transfer calculations, wax deposition modeling was performed with both lab and field scale operating conditions to understand the different roles of the water phase on wax deposition. The following impacts of the water phase on the wax deposition characteristics were discovered.

- In lab scale simulations, wax deposition rate decreases with increases water volume fraction in the bulk because of the expansion of thermal boundary layer associated with the increase in the fluid viscosity when water is dispersed in oil.
- On the contrary, in field scale simulations, wax deposition rate increases with increasing water volume fraction in the feed as the water phase preserves heat and the concentration driving force for deposition due to its high heat capacity.
- The wax deposition rate also increases with increasing droplet diameter. When the droplet size is comparable or larger than that of the mass transfer boundary layer, the mass transfer within the boundary layer is not hindered as profoundly as when the droplet size is much smaller than the boundary layer thickness.

## Acknowledgment

The authors would like to thank the financial support from the University of Michigan Industrial Affiliates Sponsors: AssuredFlowSolutions LLC., BP, Chevron, ConocoPhillips, Multichem a Halliburton Service, Phillips66, Statoil and Total.

## Literature Cited

1. Niesen VG. The real cost of subsea pigging. *E&P Mag*. 2002;97. Available online: <http://www.epmag.com/archives/features/3332.htm>
2. Svendsen JA. Mathematical modeling of wax deposition in oil pipeline systems. *AIChE J*. 1993;39(8):1377–1388.
3. Creek J, Lund HJ, Brill JP, Volk M. Wax deposition in single phase flow. *Fluid Phase Equilib*. 1999;158-160:801–811.
4. Lindeloff N, Krejbjerg K. A compositional model simulating wax deposition in pipeline systems. *Energy Fuels*. 2002;16(4):887–891.
5. Ramirez-Jaramillo E, Lira-Galeana C, Manero O. Modeling wax deposition in pipelines. *Pet Sci Technol*. 2004;22(7-8):821–861.
6. Huang Z, Lee HS, Senra M, Scott Fogler H. A fundamental model of wax deposition in subsea oil pipelines. *AIChE J*. 2011;57(11):2955–2964.
7. Huang Z, Lu Y, Hoffmann R, Amundsen L, Fogler HS. The effect of operating temperatures on wax deposition. *Energy Fuels*. 2011;25(11):5180–5188.

8. Lu Y, Huang Z, Hoffmann R, Amundsen L, Fogler HS. Counterintuitive effects of the oil flow rate on wax deposition. *Energy Fuels*. 2012;26(7):4091–4097.
9. Zheng S, Zhang F, Huang Z, Fogler HS. Effects of operating conditions on wax deposit carbon number distribution: theory and experiment. *Energy Fuels*. 2013;27(12):7379–7388. doi:10.1021/ef402051n.
10. Edmonds B, Moorwood T, Szczepanski R, Zhang X. Simulating wax deposition in pipelines for flow assurance. *Energy Fuels*. 2008;22(11):729–741.
11. Shi H, Cai J, Jepson WP. Oil-water two-phase flows in large diameter pipelines. *J Energy Resour Technol*. 2001;123:270–276.
12. Huang Z, Senra M, Kapoor R, Fogler HS, Lee HS. Wax deposition modeling of oil/water stratified channel flow. *AIChE J*. 2011;57(11):841–851.
13. Czarniecki J, Tchoukov P, Dabros T, Xu Z. Role of asphaltenes in stabilisation of water in crude oil emulsions. *Can J Chem Eng*. 2013;91(8):1365–1371.
14. McLean JD, Kilpatrick PK. Effects of asphaltene solvency on stability of water-in-crude-oil emulsions. *J Colloid Interface Sci*. 1997;189(2):242–253.
15. Schorling P-C, Kessel D, Rahimian I. Influence of the crude oil resin/asphaltene ratio on the stability of oil/water emulsions. *Colloids Surfaces A Physicochem Eng Asp*. 1999;152(1-2):95–102.
16. Xia L, Lu S, Cao G. Stability and demulsification of emulsions stabilized by asphaltenes or resins. *J Colloid Interface Sci*. 2004;271(2):504–506.
17. Bruno A, Sarica C, Chen H, Volk M. Paraffin Deposition During the Flow of Water-in-Oil and Oil-in-Water Dispersions in Pipes. In: *2008 SPE Annual Technical Conference and Exhibition*. Denver, CO: Society of Petroleum Engineers, 2008.
18. Zhang Y, Gong J, Ren Y, Wang P. Effect of emulsion characteristics on wax deposition from water-in-waxy crude oil emulsions under static cooling conditions. *Energy Fuels*. 2010;24(2):1146–1155.
19. Aichele CP, Chapman WG, Rhyne LD, Subramani HJ, House WV. Analysis of formation of water-in-oil emulsions. *Energy Fuels*. 2009;23(13):3674–3680.
20. FLUENT User Guide, 2004, Published by ANSYS, Inc.
21. ANSYS CFX\_Solver Modeling Guide, 2009, Published by ANSYS, Inc.
22. Oosthuizen PH, Naylor D. *An Introduction to Convective Heat Transfer Analysis*. New York: WCB/McGraw Hill, 1999.
23. Chang J, Wang G, Gao J, Zhang K, Chen H, Yang Y. CFD modeling of particle-particle heat transfer in dense gas-solid fluidized beds of binary mixture. *Powder Technol*. 2012;217:50–60.
24. Choi HS, Meier D. The characteristics of gas–solid flow and wall heat transfer in a fluidized bed reactor. *Heat Mass Transf*. 2012;48(9):1513–1524.
25. Hamzehei M, Rahimzadeh H. Experimental and numerical study of hydrodynamics with heat transfer in a gas - solid fluidized-bed reactor at different particle sizes. *Ind Eng Chem Res*. 2009;48(6):3177–3186.
26. Yusuf R, Halvorsen B, Melaaen MC. Eulerian–Eulerian simulation of heat transfer between a gas–solid fluidized bed and an immersed tube-bank with horizontal tubes. *Chem Eng Sci*. 2011;66(8):1550–1564.
27. Zheng S, Fogler HS. Fundamental investigation of wax diffusion characteristics in water-in-oil emulsion. *Ind Eng Chem Res*. 2015;54(16):4420–4428.
28. Grace HP. Dispersion phenomena in high viscosity immiscible fluid systems and application of static mixers as dispersion devices in such systems. *Chem Eng Commun*. 1982;14(3-6):225–277.
29. Hinze JO. Fundamentals of the hydrodynamic mechanism of splitting in dispersion processes. *AIChE J*. 1955;1(3):289–295.
30. Brauner N. The prediction of dispersed flows boundaries in liquid-liquid and gas-liquid systems. *Int J Multiph Flow*. 2001;27:885–910.
31. Cai J, Li C, Tang X, Ayello F, Richter S, Nescic S. Experimental study of water wetting in oil-water two phase flow - horizontal flow of model oil. *Chem Eng Sci*. 2012;73:334–344.
32. Maxwell CA. *Treatise on Electricity and Magnetism*, 3rd ed. New York: Dover Publications, 1954.
33. Singh A, Lee H, Singh P, Company C, Sarica C. OTC 21641 SS: Flow Assurance: Validation of Wax Deposition Models Using Field Data from a Subsea Pipeline. In: *Offshore Technology Conference*. Houston, TX: Offshore Technology Conference, 2011.
34. Hoffmann R, Amundsen L. Single-phase wax deposition experiments. *Energy Fuels*. 2010;24(2):1069–1080.
35. Panacharoensawad E, Sarica C. Experimental study of single-phase and two-phase water-in-crude- oil dispersed flow wax deposition in a mini pilot-scale flow loop. *Energy Fuels*. 2013;27(9):5036–5053.
36. Panacharoensawad E. Wax deposition under two-phase oil- water flowing conditions. Ph.D. Dissertation, The University of Tulsa, Tulsa, OK, 2012.
37. Venkatesan R, Fogler HS. Comments on analogies for correlated heat and mass transfer in turbulent flow. *AIChE J*. 2004;50(7):1623–1626.
38. Alder BJ, Wainwright TE. Phase transition for a hard sphere system. *J Chem Phys*. 1957;27(5):1208–1209.
39. Wood WW, Jacobson JD. Preliminary results from a recalculation of the monte carlo equation of state of hard spheres. *J Chem Phys*. 1957;27:1207.
40. Couto GH, Chen H, Dellecase E, Sarica C, Volk M. An investigation of two-phase oil/water paraffin deposition. In: *2006 Offshore Technology Conference*. Houston, TX: Offshore Technology Conference, 2008.

*Manuscript received Sep. 8, 2016, and revision received Mar. 6, 2017.*